Plasma Physics and Controlled Fusion

PAPER • **OPEN ACCESS**

Experimental and numerical characterization of a radio-frequency plasma source with a DC-grounded electrode configuration using a quarter-wavelength filter

To cite this article: Kunal Soni *et al* 2021 *Plasma Phys. Control. Fusion* **63** 045005

OPEN ACCESS
IOP Publishing
Plasma Physics and Controlled Fusion
Plasma Phys. Control. Fusion **63** (2021) 045005 (16pp)
https://doi.org/10.1088/1361-6587/abdbd1

Experimental and numerical characterization of a radio-frequency plasma source with a DC-grounded electrode configuration using a quarter-wavelength filter

Kunal Soni[1], Lucas Moser[1], Zoltán Donkó[2], Peter Hartmann[2], Ihor Korolov[3], Rodrigo Antunes[1], Zoltan Juhasz[4], Roland Steiner[1], Laurent Marot[1] and Ernst Meyer[1]

[1] Department of Physics, University of Basel, Klingelbergstrasse 82, CH-4056 Basel, Switzerland
[2] Wigner Research Centre for Physics, 1121 Budapest, Hungary
[3] Ruhr-Universität Bochum, Universitätsstrasse 150, 44801 Bochum, Germany
[4] Department of Electrical Engineering and Information Systems, University of Pannonia, 8200 Veszprém, Hungary

E-mail: kunaldhirajal.soni@unibas.ch

Received 21 September 2020, revised 18 December 2020
Accepted for publication 14 January 2021
Published 11 February 2021

Abstract

We present a combined experimental and numerical investigation of the plasma properties in an asymmetric capacitively coupled radio frequency plasma source using argon discharge. Besides driving the system in the conventional way, which results in a high negative self-bias voltage V_{DC} due to the asymmetric configuration, we also connect a 'quarter-wavelength filter' to the powered electrode, which lifts its DC potential to zero. At the powered side of the plasma, we employ electrodes with conducting and insulating surfaces, as well as electrodes combining both in different proportions ('hybrid electrodes'). Measurements are carried out for the plasma potential, the electron density and temperature in the bulk plasma, as well as for the flux-energy distribution of the ions at the grounded surface of the system. The nature of the surface of the powered electrode as well as the presence of the quarter-wavelength filter are found to highly influence the plasma potential, $\overline{V_p}$. For the electrode with a conducting surface $\overline{V_p} \sim 20$ V and $\sim$150 V are found in the absence and the presence of the filter, respectively. For the electrode with an insulating surface, the self-bias voltage builds up directly at the plasma interface, thus the filter has no effect and a plasma potential of $\sim$20 V is found. For the electrodes with different conducting/insulating proportions of their surface, $\overline{V_p}$ ranges between the above values. Particle-in-Cell/Monte Carlo Collisions calculations for identical conditions with hybrid electrodes predict double-peaked ion energy distribution at the powered electrode with peaks corresponding to $e\overline{V_p}$ and $e(\overline{V_p} - V_{DC})$ along with a lowering of the plasma potential (when

compared to wholly conducting electrode), a trend that is observed experimentally. These studies are of great importance for the application of similar plasma sources with *in-situ* cleaning of mirrors in fusion devices and the results can be extended to a variety of plasma processing applications.

Keywords: RF plasma, DC-grounded electrodes, ITER, plasma-surface interactions, notch filter

(Some figures may appear in colour only in the online journal)

1. Introduction

Capacitively coupled plasma (CCP) sources have a variety of important applications, which make use of the interaction of active species (ions and radicals) created in the plasma volume with the surface materials of the electrodes. Due to the radio-frequency (RF) excitation the electrode materials are not restricted to be conducting, as RF current can flow through dielectric materials as well. This tremendously widens the area of applications. Under energetic ion bombardment materials can be selectively removed using such plasma sources (e.g. Si and SiO_2 etching in microelectronics), while at low energies deposition processes may be utilized (e.g. creation of amorphous Si layers for photovolatic devices). The microstucture and wetability of surfaces can be modified as well which is of paramount importance for medical implants [1–4].

For all the above mentioned applications, the ion flux-energy distribution function, commonly called the 'ion energy distribution function' (IEDF), at the surfaces is a crucial feature. Together with the type(s) of ions, the IEDF primarily defines the processes that take place at the surface. The shape of the IEDF is determined by two important parameters: (a) the collisionality of the sheath that forms near the electrodes and (b) the relation between the ion transit time and the period of the RF excitation (see e.g. [5–7]). At high pressures, the sheaths are generally highly collisional and most of the ions have a low energy upon arrival at the electrode surfaces. At low pressures, on the other hand, the ions have a long free path and can acquire high energies while traversing the sheaths. In the latter case, assuming that the ions fly through the sheaths in a fraction of the RF period, their energy is determined by the instantaneous sheath voltage. In the opposite case, i.e. when the ion transit time is much longer than the RF period the ion energy is largely determined by the time-averaged sheath voltage. To provide more degrees of freedom for the control of the IEDF, concepts for driving voltage waveforms with two or multiple RF components with distinct frequencies have been developed [8–11].

RF plasma sources are commonly operated with a generator from which the power is coupled into the plasma via an impedance matching network that ensures optimum power transmission to the plasma. An additional element in the driving circuit (which may be part of the matching box) is a blocking capacitor that prohibits the flow of a DC current in the circuit, e.g. [1]. Whenever a plasma asymmetry is present this capacitor charges up to equalize the time-averaged fluxes of positive and negative charge carriers to any of the electrodes. According to Kirchhoff's law, for such conditions a 'self-bias voltage', V_{DC}, has to build up over the plasma to oppose the DC voltage drop over the blocking capacitor. Plasma asymmetry can be caused both by uneven areas of the powered and grounded electrodes and/or by specific multi-harmonic excitation waveforms [10–13]. The self-bias voltage has an influence on the flux-energy distribution of the ions, as it contributes to potential difference between the bulk plasma and the electrode surface, i.e. the sheath voltage drop.

For plasma sources with largely uneven powered and grounded surfaces (where usually the powered electrode is much smaller than the grounded surface), a significant negative self-bias voltage develops and the plasma potential is lower as compared to that in symmetrical systems. The plasma properties and the IEDF can be influenced by applying a DC excitation besides the RF excitation. Such RF+DC plasma sources have been studied extensively [14–17]. An alternative, straightforward way to eliminate the self-bias voltage is to ground the powered electrode for the DC component. Of the many ways to DC-ground the powered electrode [18–20], one is to use a 'stop band quarter lambda filter', also known as 'notch filter' [21]. To realize a notch filter, a transmission cable with a length of a quarter of the RF wavelength is short-circuited at one end, while the other end is connected in parallel to the powered electrode. The connection segment has, in principle, an infinite impedance at the RF frequency at the feed point, and the wave from the generator propagates unaffected to the powered electrode. At the same time, however, the DC potential of the powered electrode is set to zero by the short-circuited end of the filter. Both approaches mentioned above work only if the surface of the powered electrode is conducting.

DC grounding the powered electrode has strong implications on the plasma properties and leads to an increase of the plasma potential to several hundreds of volts (as compared to few tens of volts commonly observed in typical highly asymmetric CCPs); this has been observed experimentally in the past [22, 23]. Köhler *et al* explained the phenomenon in 1985 using a model assuming capacitive sheaths [23, 24]. According to their model, the mean (i.e. time-averaged) plasma potential, $\overline{V}_p$, for an asymmetric configuration depends significantly on the DC bias and the sheath capacitances at the powered and grounded electrodes. For a DC-grounded electrode system where the DC bias voltage is zero, the development of the plasma potential depends only on the sheath capacitances. Further, it can be concluded from the model that if the powered electrode area is much smaller than that of the grounded wall, the mean plasma potential reaches the order of the RF voltage amplitude. Aanesland *et al* developed an analytical model of

DC-grounded powered electrode discharges for a combination of capacitive and resistive sheaths taking into consideration the direct current flowing in the system [25]. They found that the plasma potential developing in a DC-grounded asymmetric electrode system depends strongly on the ratio of the grounded electrode (A_g) and powered electrode (A_p) areas. Further, the DC current was found to be limited by the flow of ions collected by the grounded electrode over an entire RF cycle. In another paper, Aanesland *et al* reported that the plasma potential with DC-grounded RF excitation was equal to the sum of plasma potential and DC self-bias on the electrode when it was excited with a floating powered electrode [26]. Recently, Faudot *et al* also published results about the properties of directly coupled plasma in ALINE [18]. They observed a linear increase in the plasma and floating potentials with an increase of the applied RF voltage amplitude till a certain point beyond which they attained a saturation. They also concluded that the average RF sheath thickness at the DC-grounded electrode was at least three times higher than the one calculated with Child–Langmuir law in a low collisional helium plasma.

The high plasma potential associated with the DC-grounded RF plasma is also responsible for the often observed phenomenon of micro-arcing [27–29]. It is attributed to the sheath breakdown at the vacuum chamber wall as a result of an increase in the plasma and floating potentials [25, 26]. The micro-arcs lead to the release of a large amount of energy over a small area in an interval of less than 1 ms at the chamber wall. Such discharges can damage sensitive electrical components and interfere with the measurements since they affect the bulk plasma parameters, and are generally considered parasitic. Few studies have investigated techniques to reduce the high plasma potential and the ensuing micro-arcs associated with DC-grounded electrodes in CCP [19, 30, 31]. In light of our article, the work conducted by Sugai *et al* is particularly relevant, where they coated the DC-grounded metal electrode with a dielectric which resulted in a DC self-bias formation on the dielectric [30].

RF discharges with DC-grounded powered electrodes are foreseen to find important applications in the diagnostic systems of nuclear fusion devices such as ITER [32, 33]. Most optical diagnostic systems in ITER will be equipped with metallic first mirrors (FMs) directing light from the hot plasma into the diagnostic while also preventing these from the energetic neutrons from the fusion plasma at the same time. The FMs, being the initial elements in the optical path in the diagnostic systems, will be subjected to deposition of the first wall materials (Be and W), which would severely compromise their optical properties. The FMs would thus require regular cleaning to restore their optical properties, for which an *in-situ* plasma cleaning technique with RF discharges is a preferred option [32]. In addition to the parasitic deposition, the FMs would also be exposed to high thermal loads caused by neutron and gamma irradiation, for which the mirrors would be actively water-cooled. However, the water cooling lines are metallic and their physical contact with the FMs leads to RF grounding. Furthermore, ceramics cannot be installed between the water pipes and the FMs in ITER, to decouple the ground from the RF. Hence, the cooling lines are foreseen to be implemented in a lambda-quarter scheme to allow decoupling of RF from the grounded cooling pipes [33]. Of the several studies discussing the plasma cleaning of FMs [34, 35], only a few have been reported about plasma cleaning of FMs in the presence of a notch filter. Dmitriev *et al* published promising results about the feasibility of the water cooling lines implemented as notch filter for ITER FMs using 81.36 MHz RF neon discharge at 1 Pa [20]. They demonstrated that Al/Al_2O_3 deposits (used as a proxy for Be/BeO deposits [36]) could be removed from the water cooled mirror surface by 100 eV Ne^+ ions at a 4 W cm^{-2} surface power density. Chen *et al* also reported mirror cleaning with discharges employing a notch filter in the EAST tokamak [37]. Successful cleaning tests with DC grounding of the powered electrode were also reported by Moser *et al* [35].

While there have been studies (like the ones mentioned above) on the applicability of DC-grounded electrodes in mirror cleaning, there has been limited research focused on the plasma physics behind this application. In this article, we use experiments and kinetic simulations to study the impact of the DC grounding of the powered electrode, realized with a notch filter, on the properties of the plasma. We also study the influence of the conducting properties of the powered electrode's surface on the resulting plasma properties: besides testing conductive and dielectric surfaces we also study electrodes of which the surface is partitioned into conducting/insulating parts with given percentages.

2. Experimental

2.1. Experimental setup

The experiments were performed at the University of Basel in Switzerland. A 13.56 MHz RF generator (Huttinger Elektronik GmbH and Co KG, model PFG 300 RF) coupled with a matchbox (Huttinger Elektronik GmbH and Co KG, model PFM 1500A) was used to generate the plasma in argon gas in a high vacuum chamber. The matchbox is composed of internal capacitors and inductors, wherein the capacitance can be tuned to match the load with the applied RF power. One of the capacitors blocks the path for a DC current, therefore no additional external blocking capacitor was required in the electrical circuit. The setup is shown schematically in figure 1 and the CAD image of the plasma chamber is displayed in figure 2.

The characteristics of the plasma were measured using a Langmuir probe (Hiden's ESPion^{TM}), a retarding field energy analyzer (RFEA) (manufactured by Impedans), a sensor for current measurement and a sensor to measure the peak-to-peak value of the driving voltage ($V_{p\text{-}p}$), as discussed in more details in section 2.2.

The area A_p of the powered electrode was 5.5×10^{-3} m^2, while the entire vacuum chamber served as the grounded electrode. Accordingly, the ratio of the grounded to the powered surfaces was $A_g/A_p \approx 87$, which made the discharge highly asymmetric. The feedthrough for the RF power was positioned at the top of the chamber such that the electrode surface was centered and faced only half of the chamber (figure 2). The

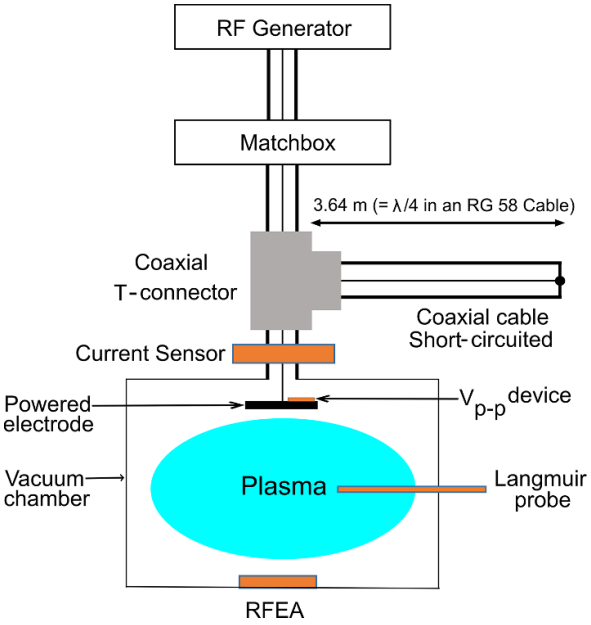

Figure 1. Schematic representation of the experimental setup. The plasma is generated inside a high-vacuum chamber using a 13.56 MHz generator with a matchbox and the notch filter connected to the powered electrode via a coaxial T-connector. The characterization devices (Langmuir probe, RFEA, current sensor and $V_{p\text{-}p}$ device) are shown in orange.

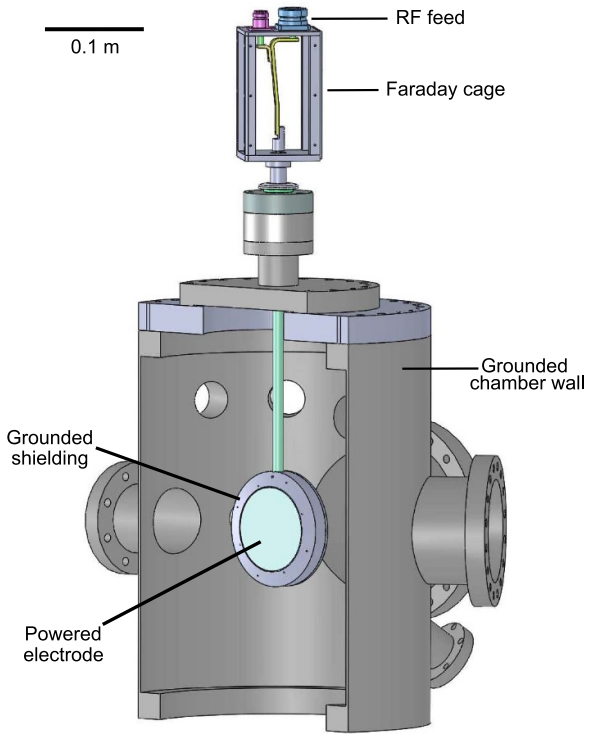

Figure 2. CAD image of the experimental setup showing the powered electrode surrounded by a shielding in the centre of the cylindrical vacuum chamber which serves as the grounded electrode.

distance between the electrode surface and the grounded wall was 114 mm.

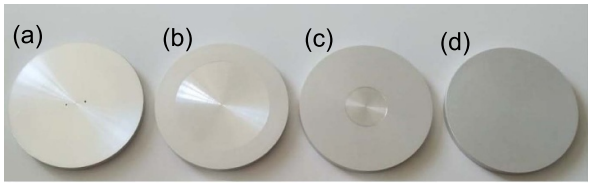

Figure 3. Samples used as powered electrode in the experiments. (a) 100% metallic, (b) 50% metallic, (c) 10% metallic, (d) 0% metallic.

Table 1. Discharge parameters in the experiments.

Experimental parameters	Value
Area of powered electrode A_p	5.5×10^{-3} m^2
Area of the grounded chamber A_g	4.8×10^{-1} m^2
Ar pressure	1 Pa
Driving frequency	13.56 MHz
RF voltage amplitude	180 V

Due to the large disparity of the powered vs. the grounded surface areas, a strong negative self-bias is established at the powered electrode in the absence of DC grounding. This self-bias was, however, suppressed by using a quarter-wavelength notch filter made of an RG 58-type coaxial cable. As the wave propagation speed is decreased in the cable compared to that in vacuum, the proper length of the filter cable (3.64 m) was defined by accounting for a reduction factor of ≅0.66 [38]. This filter was connected to the RF feed line by a T-connector, while its other end was short-circuited (see figure 1).

The experiments were carried out with four aluminum (Al) disks having a diameter of 84 mm and different conducting/insulating areas. In the case of one electrode (or 'sample') a full metallic surface was preserved (and was ensured in the discharge by the bombardment of energetic ions at the low operating pressure). For the other electrodes, the surface was covered with a 10 μm thick Al_2O_3 dielectric film via anodization of the Al disks. The dielectric breakdown voltage of the Al_2O_3 film was found to be much larger than 200 V, ensuring that the film remains an insulating dielectric under the potentials of interest. One of the samples was operated covered completely with Al_2O_3 film, while for the others the oxide layer was subsequently partly removed so that different metallic/dielectric (Al/Al_2O_3) proportions of the surface were obtained. Consequently, electrodes with metallic proportions between 0% and 100%, as shown in figure 3, were produced. Electrodes having both types of surfaces are referred to as 'hybrid' electrodes hereon. The thickness of the dielectric coating ensured that ion bombardment did not remove it during the discharge.

The experimental conditions are presented in table 1.

2.2. *Characterization techniques*

The electron temperature T_e, plasma potential $\overline{V_p}$, electron density n_e and floating potential V_f of the bulk plasma were measured using Hiden's ESPion^{TM} Langmuir probe [39]. MK2 platinum probe tips with a length and diameter of 10 mm and 0.15 mm, respectively, were used for the measurements.

Table 2. Plasma parameters: floating potential (V_f), plasma potential ($\overline{V_p}$), electron temperature (T_e), and electron density (n_e) for the set of conditions given in table 1, evaluated by the ESPion software, Chen's method, and the *I*-squared method.

Method	V_f (V)	$\overline{V_p}$ (V)	T_e (eV)	n_e (m^{-3})
ESPion	108	112	2.6	3.6×10^{15}
Chen	108	113	2.7	1.7×10^{15}
I-squared	—	—	—	1.7×10^{15}

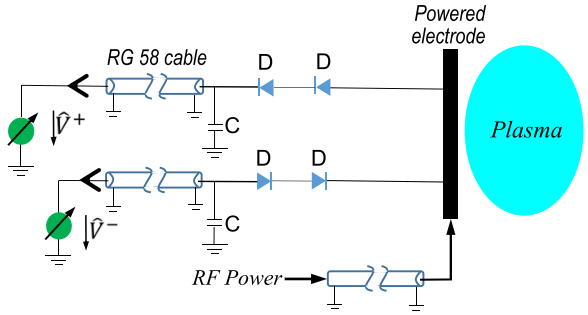

Figure 4. Circuit diagram of the peak-to-peak voltage ($V_{p\text{-}p}$) measurement device. The capacitance C was 1 nF/3 kV and the diode D used was MUR1100E (Power Rectifier, Ultra-Fast Recovery, Switch-mode, 1 A, 1000 V). The positive ($\widehat{V^+}$) and negative ($\widehat{V^-}$) peak voltages are measured with the voltmeters.

The commercial probe has a measuring range of −200 V to 100 V to obtain the *I*–*V* curve. Since the experiments required measurements beyond a probe voltage of 100 V, the entire Langmuir probe head and its power supply were electrically floated to shift the scanning range by +100 V. The probe tip was positioned in the quasineutral bulk plasma region, at 4 cm from the surface of the powered electrode.

To obtain the plasma parameters (T_e, n_e and $\overline{V_p}$), the measured $I-V$ curves were fitted using the ESPionSoft™ software. Moreover, the measurements were also manually evaluated using the Chen method [40] as well as the *I*-squared method [41]. Exemplary results corresponding to the RF voltage amplitude of 180 V and Ar pressure of 1 Pa are presented in table 2.

While the Chen method allows for calculation of T_e, n_e and $\overline{V_p}$ from the *I*–*V* curve, the *I*-squared method is used solely for the determination of n_e while avoiding calculations of T_e and $\overline{V_p}$ from the electron saturation current. All three procedures give similar results as observed in table 2 with the exception of n_e, of which a higher value was obtained by the ESPion software in comparison to the others. Chen and *I*-squared methods were adopted for the *I*–*V* curve analysis throughout this paper, since they are more effective in reducing the noise in the data at low pressures and also due to the fact that the n_e obtained by the two methods were close to each other.

The current density and energy of the ions reaching the wall of the chamber were measured using a SEMion™ single sensor RFEA manufactured by Impedans, Ltd [42, 43]. The RFEA measurements were analyzed using the Semion System™ software to obtain the ion current density (J_i) and the mean ion energy (E_{ion}). The typical uncertainties for the measurements in J_i and E_{ion} as provided by Impedans, Ltd are ±20% and ±2% (in addition to ±1 eV resolution), respectively. While it was not possible to measure the energy distribution of the ions at the powered electrode, the same information at the grounded surface provides the useful possibility of comparison with simulation results.

The discharge current was monitored by a current sensor mounted at the RF feed line using a T-connector (figure 1). The uncertainty of measurement of the current sensor was ±2 mA. Lastly, a device for the measurement of the peak-to-peak voltage was connected to the powered electrode (figure 4). The voltages were measured by DC voltmeters connected via electrical feedthroughs to the measuring circuit.

3. Simulation method and input values

The experimental results are compared with those obtained from particle based kinetic simulations performed at the Wigner Research Centre for Physics in Budapest, Hungary, using a two-dimensional axisymmetric, electrostatic Particle-in-Cell/Monte Carlo Collisions (PIC/MCC) code. The basics of the PIC/MCC approach are not discussed here, these can be found in numerous works in the literature [44–51].

The cylindrical geometry was parametrized with the (z, r) coordinates and assumed a chamber with a radius of $R = 216$ mm and a height of $H = 114$ mm. All surfaces were assumed to be metallic and electrically grounded except for the powered electrode, which was situated in the center of one of the flat ends at $z = 0$ and has a diameter of $R_e = 42$ mm. This geometry was chosen to replicate the experimental system (figure 2) by providing: (a) the same distance between the powered electrode and the facing wall and (b) an equivalent ratio of the grounded and powered surfaces $A_g/A_p = 80$, while providing compatibility with the cylindrical symmetry required by the numerical scheme.

In the PIC/MCC simulation, electrons and Ar^+ ions are traced and their collisions with the background Ar gas atoms are taken into account. Details of the numerical method are provided in [44] and references therein. In the present study a simplified collision process set was used for the electrons, where elastic, excitation and ionization channels were represented by the ε impact energy dependent cross sections $\sigma_{ela}(\varepsilon)$, $\sigma_{exc}(\varepsilon)$ and $\sigma_{ion}(\varepsilon)$ as provided in [52], all assuming isotropic scattering distributions. In the case of Ar^+ ions, the cross sections were adopted from [53] for the isotropic and back-scattering elastic channels, and from [54] for the excitation and ionization processes.

In the model, an electron reflection probability $\eta = 0.5$ and an ion induced electron emission yield $\gamma = 0.1$ were included at the electrodes. Such simplified surface models can be used in cases where the plasma parameters show weak sensitivity on the actual values of these parameters, in contrast to cases (typically using higher voltages), where surface processes are of key importance for the overall charge production, as shown in [55]. Performing simulations for the present conditions, however, with different values for the ion induced electron emission yield showed only marginal effects on the computed

plasma parameters. The self consistent electric field was computed in every time-step by solving the Poisson equation on a numerical grid implementing the parallel red-black successive over-relaxation method as discussed in [56]. The driving RF voltage had a base frequency $f_{RF} = 13.56$ MHz and was applied as time-dependent boundary condition to the powered electrode in the form:

$$V(t,r) = V_{RF}\cos(2\pi f_{RF}t) + V_{DC}(r), \quad (1)$$

where V_{RF} is the RF voltage amplitude and V_{DC} is the optional DC self-bias voltage. In case of the conductive regions of the electrode $V_{DC} = 0$ V was used, while in case of insulating surfaces V_{DC} was iteratively approximated by the simulation code so that a value providing a balance between the time-averaged electron and ion currents to the insulating electrode area was found. The simulations include all electrode configurations that were available in the experiment, as discussed in section 2.1. The dependence of V_{DC} on the coordinate r that appears in equation (1) allows a position dependent self-bias voltage to build up over different regions of the hybrid electrodes. The parameters used for the simulations are collected in table 3.

The numerical parameters of the simulations, such as the size of the numerical grid, the duration of the individual time-steps, and the choice of the super-particle weight factor, which represent the number ratio between the real microscopic particles and the simulation ('super-') particles were set by fulfilling the general stability criteria of the PIC/MCC scheme as discussed, e.g. in [51]. As a result, two-dimensional PIC/MCC simulations turn out to be extremely computational intensive, and in contrast to one-dimensional cases, are not practical if implemented as a sequential code running on a single CPU core. As an illustration of the computational cost, the execution of the simulation of a similar system using a parallel MPI (message passing interface) implementation took three months for 10^7 super-particles on an 8-processor (Intel Xeon-8850 CPUs) shared memory architecture running on 24 cores. To improve upon these run-times we decided to use high-performance GPUs (graphics processing units) with a massively parallel implementation of the simulation code. This way the motion and collisions of thousands of particles are computed at the same time, as well as the solution of the Poisson equation is largely accelerated.

GPUs are designed to be able to hold the state of a large number of threads on-chip, making thread-switching practically zero cost. As a result, up to 10^5–10^6 threads can be executed efficiently, without overheads. To achieve maximum flexibility and hardware efficiency, the program was implemented in CUDA-C with custom parallel kernels. Since PIC/MCC codes are typically memory bound (the number of executable instructions in the algorithm is less than what the chip can execute in the time of the required memory data transfers), our implementation was optimized to make best use of fast on-chip memory during calculation. The resulting implementation could achieve a speedup factor of about 100 with respect to our earlier, CPU based parallel version.

Table 3. Input parameters used for the PIC/MCC simulations.

Simulation parameters	Value
Area ratio of the electrodes A_g/A_p	80
Ar pressure	1 Pa
Driving frequency	13.56 MHz
RF amplitude (V_{RF})	180 V
Gas temperature	350 K
Electron reflection coefficient	0.5
Ion induced electron emission yield	0.1
Computational grid (z, r)	512×1024

4. Results and discussion

The experimental and simulation results for the plasma characteristics obtained with powered electrodes having different surface properties (figure 3) are presented in this section. The results obtained for electrodes with different surface characteristics (i.e. conducting, insulating, and hybrid) are discussed in separate subsections. Some of the presented figures display data for all the electrodes, to aid the comparison between the various cases.

4.1. Conducting electrode

A reference experiment with $V_{RF} = 180$ V RF voltage amplitude and $p = 1$ Pa argon pressure, without applying the notch filter was performed with the electrode having 100% conducting area (figure 3(a)). In the absence of the notch filter, no DC current can flow in the external circuit because of the presence of the blocking capacitor. As a result of the large difference between the powered and grounded surface areas, a high negative self-bias of -156 V formed at the powered electrode. For these conditions the plasma potential (as inferred from the Langmuir probe data) was found to be $\overline{V_p} \approx +20$ V and a value of $n_e = 8.6\times10^{14}$ m^{-3} was obtained for the electron density.

However, when the plasma was driven with DC grounding of the powered electrode with the notch filter, $\overline{V_p}$ increased to 151.6 V for the same RF voltage amplitude. For this case, T_e and n_e were found to be 3.2 eV and 1.8×10^{15} m^{-3}, respectively. The applied RF power density on the powered electrode was 0.3 W cm^{-2}.

The high $\overline{V_p}$ obtained can be understood using the capacitive sheath model for DC-grounded electrodes [23, 24]. The time varying voltage $V(t)$ on the RF driven electrode is given by equation (1). For a general case, where a net current is possible through the powered electrode, the mean plasma potential $\overline{V}_p$ is given by:

$$\overline{V}_p = V_{DC} + V_{RF}\frac{C_g}{C_p + C_g}, \quad (2)$$

where C_g and C_p are the time-averaged sheath capacitances at the grounded wall and the powered electrode, respectively. If the powered electrode is DC-grounded, V_{DC} is zero and equation (2) reduces to

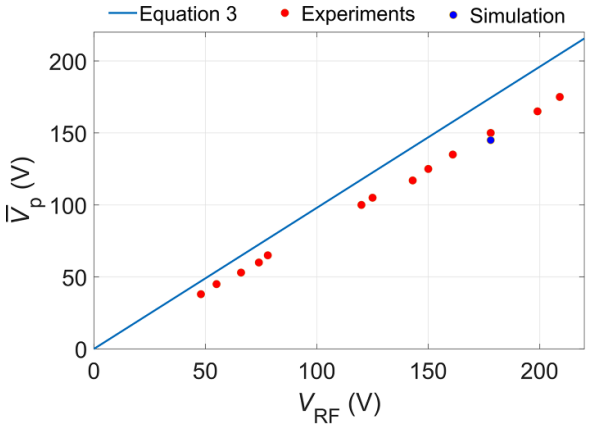

Figure 5. Comparison of theoretical (equation (3)) and experimentally observed $\overline{V_p}$ for the applied V_{RF}. The L_{sh} corresponding to the capacitances C_g and C_p have been assumed identical, reducing the ratio of capacitances $C_g/(C_g + C_p)$ to simply ratio of areas $A_g/(A_g + A_p)$ in equation (3). $\overline{V_p}$ obtained from the simulations for $V_{RF} = 180$ V is also presented for comparison.

$$\overline{V_p} = V_{RF}\frac{C_g}{C_p + C_g}. \tag{3}$$

The magnitude of the sheath capacitances in this expression can be found using the relation,

$$C = \epsilon_0 \frac{A}{L_{sh}}, \tag{4}$$

where ε_0 is the permittivity of vacuum, L_{sh} the mean sheath thickness and A the effective area of the electrode in contact with the plasma. The effective area of electrode in question may differ from the geometrical surface area of the electrode [59–61]. Using the relation of the sheath capacitances (equation (4)), equation (3) can be modified as,

$$\overline{V_p} = V_{RF}\frac{(A_g/A_p)}{(L^g_{sh}/L^p_{sh}) + (A_g/A_p)}, \tag{5}$$

where L^g_{sh} and L^p_{sh} are the sheath thicknesses at the grounded and powered electrodes, respectively. As can be observed from equation (5), $\overline{V_p}$ depends significantly on the ratio of the areas A_g/A_p, and in the limit of $A_g \gg A_p$, $\overline{V_p}$ rises to the order of V_{RF}. The ratio of the sheath thicknesses L^g_{sh}/L^p_{sh} does not play a major role in the determination of $\overline{V_p}$ in highly asymmetric DC-grounded electrode systems since A_g/A_p is one or two orders of magnitude larger than L^g_{sh}/L^p_{sh}. Equation (5) suggests that $\overline{V_p}$ increases linearly as a function of V_{RF}. This trend was confirmed experimentally as can be observed in figure 5. The small difference between the experimentally observed $\overline{V_p}$ and that calculated from equation (3) can be attributed to the small difference that exists in the L_{sh} at the powered and grounded electrode in the experiments as well as to the fact that effective area ratio of the electrodes is lower than the geometrical area ratio of 87. The high plasma potential obtained with DC-grounded powered electrode is also in agreement with the results reported in [22–24].

The simulations corroborate the experimental observations. Figure 6 shows the potential distribution along the axis of the discharge for different scenarios. In addition to the simulation results obtained for the grounded/powered surface area approximating the experimental system ($A_g/A_p = 80$), the figure also shows data for a geometrically symmetric discharge ($A_g/A_p = 1$, figure 6(a)). In this case, no self-bias voltage was present and the plasma potential exhibited large oscillation in the bulk region, between 10 V and 191 V. In the asymmetric system ($A_g/A_p = 80$), the situation changed dramatically. Figure 6(b) shows the data obtained without DC grounding of the powered electrode. In this case a self-bias voltage of -164 V was computed, which is in fair agreement with the value obtained experimentally, $V_{DC} = -156$ V. Turning on the DC grounding of the powered electrode in the simulation re-established $V_{DC} = 0$ V, as it can be seen in figure 6(c). At the same time, the plasma potential was shifted upwards, and

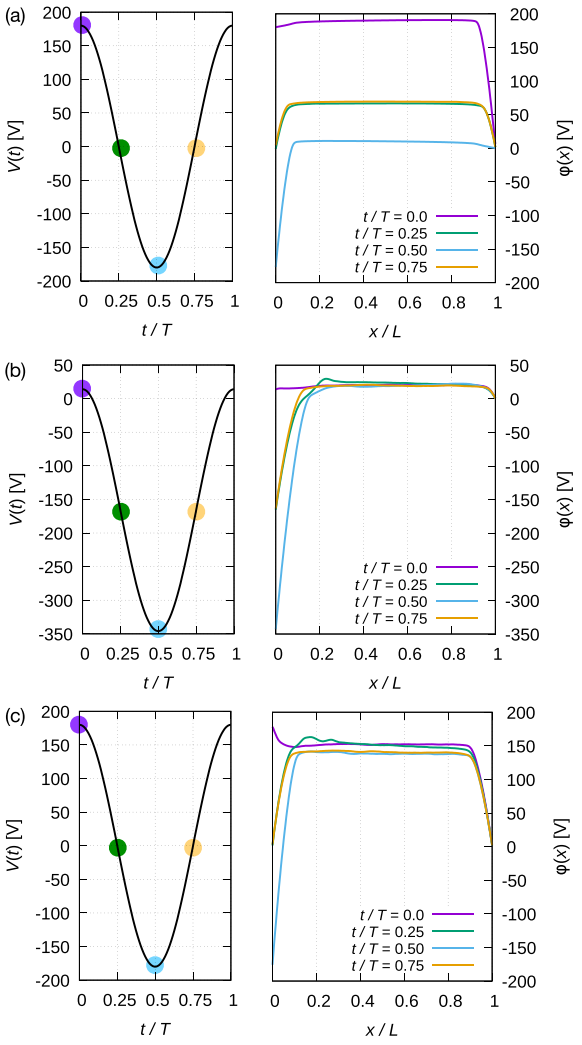

Figure 6. Simulation results for the potential of the powered electrode (left column) and computed potential distributions along the axis of the discharge (right column) in a symmetric ($A_g/A_p = 1$) system (a), and in the asymmetric ($A_g/A_p = 80$) system without (b) and with (c) DC grounding of the powered electrode. The potential distributions in the right column are shown for the times indicated by symbols with the corresponding colors in the left column. The discharge conditions are listed in table 3. The powered electrode is at $x/L = 0$ while the electrode at $x/L = 1$ is at ground potential.

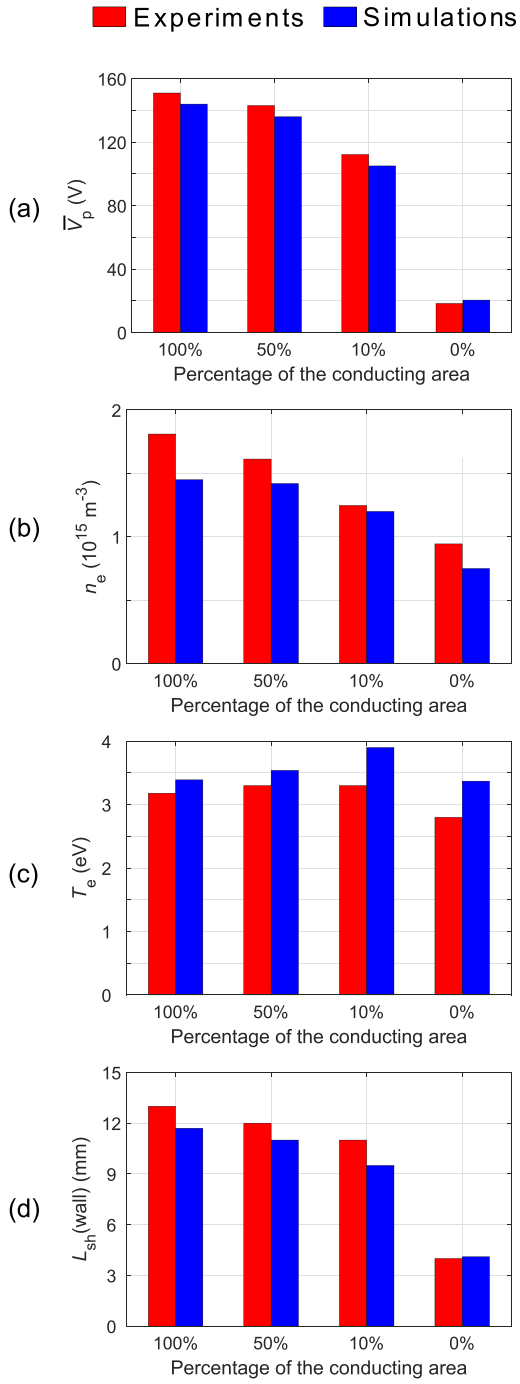

Figure 7. Comparison of experimental and simulation results for the (a) plasma potential $\overline{V_p}$, (b) electron density n_e, (c) electron temperature T_e, and (d) sheath thickness L_{sh} at the wall, for discharges with powered electrodes having different percentages of conducting surface area. The uncertainties in the experimental results are estimated at 10% for $\overline{V_p}$, 20% for n_e and T_e , and 17.5% for L_{sh} (calculated from error analysis of equation (6)).

oscillated between 138 and 152 V within the RF cycle, which is again in reasonable agreement with the value of ≈150 V obtained in the Langmuir probe measurements. The comparison of the plasma potential (including T_e, n_e and L_{sh} at the grounded wall) obtained experimentally and via simulations can be observed in figure 7.

The IEDF was measured at the grounded wall with the RFEA. The shape of the IEDF in a RF sheath depends critically on the ratio of the ion transit time across the sheath τ_i and the RF time period τ_{RF} [62]. τ_i in the collisionless, low-pressure domain can be calculated using the relation,

$$\tau_i = 3L_{sh}\left(\frac{M}{2e\overline{V}_s}\right)^{\frac{1}{2}}, \tag{6}$$

where e is the electronic charge, M the mass of ion, and $\overline{V}_s$ the mean (time-averaged) sheath voltage [1]. At high RF frequencies, $\tau_i/\tau_{RF} \gg 1$ and the displacement current in the sheath is larger than the conduction current making the sheath predominantly capacitive. At low frequencies, $\tau_i/\tau_{RF} \ll 1$ and the conduction current dominates making the sheath resistive in nature. The approximate L_{sh} in equation (6) can be calculated using the Child–Langmuir law [63, 64],

$$L_{sh} = \frac{2}{3}\left(\frac{2e}{M}\right)^{\frac{1}{4}}\left(\frac{\epsilon_0}{J_i}\right)^{\frac{1}{2}}\overline{V}_s^{\frac{3}{4}}. \tag{7}$$

The measured IEDF obtained at the grounded electrode is shown in figure 8(a). This distribution has a well-defined peak at 143.8 eV corresponding to the time-averaged sheath voltage $\overline{V}_s$. The J_i measured with the RFEA was 0.09 A m^{-2}. Using the above equations, L_{sh} and τ_i were calculated to be 13 mm and 1450 ns, respectively. For the 13.56 MHz driving frequency $\tau_{RF} = 73.75$ ns, resulting in $\tau_i/\tau_{RF} \approx 13$, implying that the sheath at the wall was primarily capacitive validating the applicability of the capacitive sheath model for our results. The ion energy distribution at the wall obtained in simulations shows very good agreement with the experimental results (figure 8(a)).

The IEDF at the powered electrode was not measured experimentally, but the simulation results show a bimodal distribution corresponding to $\overline{V}_s$ of 143 eV with an energy separation between the peaks $\Delta E \approx 10$ eV (figure 8(b)). $\overline{V}_s$ at the electrode is simply $\overline{V_p} + V_{DC}$. As $V_{DC} = 0$, $\overline{V}_s = \overline{V_p}$ which defines the high-energy limit of the ions that reach the powered electrode. Furthermore, since $L_{sh} = 13.6$ mm (as obtained from the simulations) is comparable to the mean free path of Ar ions (10.6 mm and 14.2 mm at 10 eV and 100 eV ion energies, respectively) under the conditions of the simulation, the ions may undergo few collisions within the sheath [7]. This leads to ion-neutral charge exchange collisions within the sheath resulting in a creation of slow Ar^+ ions and fast neutrals, populating the low energy part of the IEDF. The acceleration of the slow ions by the sheath electric field, which is further modulated by the plasma series resonance [57, 58], visible as vertical oscillatory features in figure 9, and the fact that even for the fastest ions it takes several RF cycles to travel L_{sh} distance, leads to the occurrence of the lower energy peaks in the IEDF as observed in figure 8(b) [5, 6]. The presence of a strong field reversal during the sheath collapse period at the powered electrode, as visible in figure 6(c) ($t/T = 0$ line) and shown in detail in figure 9(a), decelerates the arriving ions causing an increasing trend in the IEDF toward low energies.

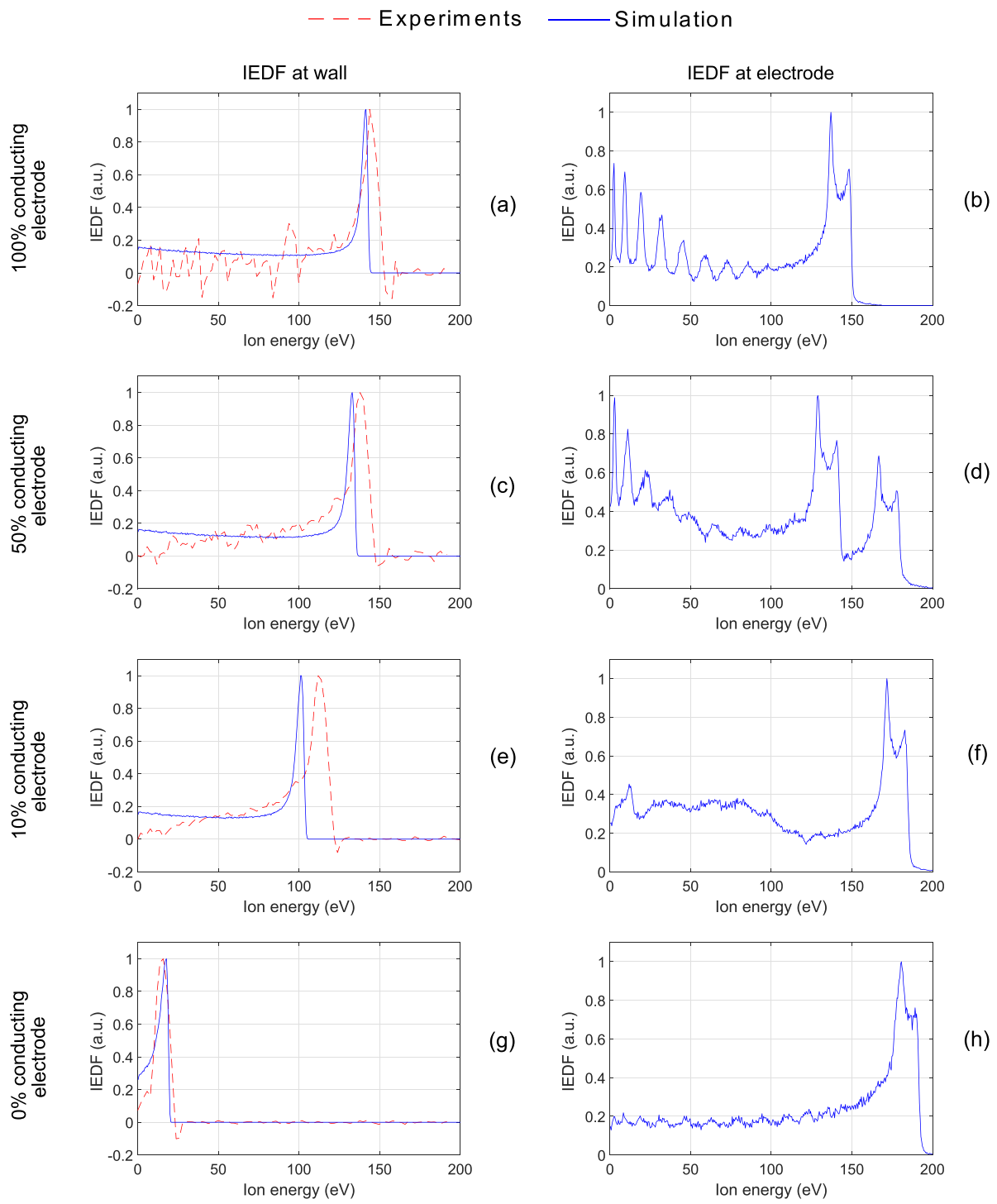

Figure 8. Experimental and computed (normalized) IEDFs of the Ar^+ ions reaching the grounded wall (left column) for the discharges with electrodes having different percentages of conducting surface: (a), (b) 100%, (c), (d) 50%, (e), (f) 10%, and (g), (h) 0%. Computational results are also shown for the powered electrode (right column).

An electric field reversal at the powered electrode develops as a result of the high plasma potential and the fact that at the grounded surfaces no sheath collapse occurs at any time, as it can be seen in figure 9(a). The space near the grounded electrode acts practically as a DC sheath preventing electrons from reaching the surface during the RF period, while efficiently extracting positively charged ions from the bulk plasma. However, in case of a stationary discharge state a balance between the production and loss of charged particles has to be established over time. The only possibility for electrons to leave the discharge is through the powered electrode during the short time of local sheath collapse, thus the electric field reversal helps to accelerate the electrons toward the electrode, which would not be able to reach the electrode only

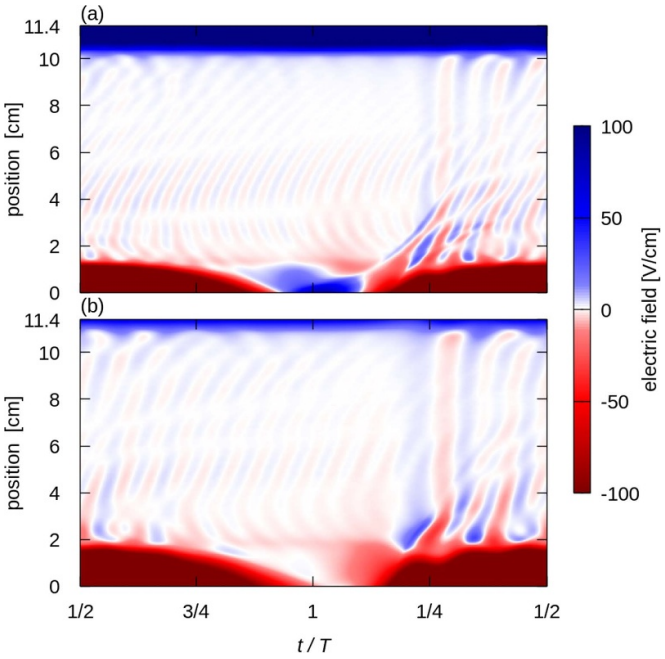

Figure 9. Computed space-, and time resolved axial electric field between the powered electrode and the facing grounded wall. The radial distribution is averaged in the range $r < R_{el}/2$, where $R_{el} = 42$ mm is the radius of the electrode, and only the axial distance from the electrode is shown on the vertical axis. The horizontal axis covers one RF period of the applied voltage as given in formula (1). Panel (a) shows results for the conducting electrode, while panel (b) depicts the insulating electrode data. Note the strong field reversal developing during the time of sheath collapse ($t/T_{RF} \approx 1$) at the powered electrode (near position 0) in the case of conducting electrode.

by diffusion in the required quantity. An indirect effect of this field reversal is the deceleration of ions on their way toward the powered electrode, as stated above. In addition to the sheath dynamics the presence of the plasma series resonance can also be observed in figure 9 as high frequency oscillating electric field features in the plasma bulk reaching into the sheath region causing additional oscillations in the energy distributions of charged particles arriving at the surfaces.

The potential and electron density maps obtained from the simulations can be seen in figure 10. The potential maps show that the bulk plasma fills most of the volume, and the sheath near the powered electrode is concentrated to a few mm width. The width of the sheath region at the corners and near the side walls is significantly longer. For the powered electrode with 100% conducting surface, a high plasma potential was present over the bulk plasma with similar sheath thicknesses at the powered and the grounded electrodes. The value of the plasma potential gradually decreases with the decrease in the percentage of the conducting area of the electrode as will be discussed in the next sections.

A sequence of additional simulations was carried out to study the effect of the area ratio, A_g/A_p, on the self-bias voltage, the plasma potential, the electron temperature and density. These results (figure A1 of the appendix) show very little sensitivity of the plasma characteristics on the surface area within this domain of highly asymmetric configurations.

4.2. Insulating electrode

In the case of an insulating electrode the flow of DC current across the plasma is blocked, and as the dielectric layer acts as a capacitor. Consequently, the build-up of a DC self-bias voltage is inevitable. At such conditions the notch filter does not play a role. As compared with the case of the fully conducting electrode, $\overline{V_p}$, n_e and T_e decreased to 18.5 V, 9.44×10^{14} m^{-3} and 2.8 eV, respectively. This behavior is in excellent agreement with the simulation results (figure 7). While the negative self-bias could not be experimentally measured, the simulation results showed a development of $V_{DC} = -167$ V on the dielectric surface of the electrode which is well visible in the potential map of the system (figure 10(g)). The low $\overline{V_p}$ measured is also comparable to the $\overline{V_p}$ of +20 V obtained by Sugai *et al* in a system employing a DC-grounded electrode covered with a thick insulator [30].

These plasma characteristics are similar to the scenario when the conducting electrode is driven without DC grounding (i.e. without the notch filter), as expected, in which $\overline{V_p} = 20$ V, $n_e = 8.6 \times 10^{14}$ m^{-3} and $T_e = 3.2$ eV were observed. The two cases differ in the sense that with a conducting electrode the external blocking capacitor charges up in the absence of a notch filter, while in the case of a dielectric surface charging occurs right at the electrode surface.

The measured IEDF at the wall for this configuration exhibits a single peak at 15.8 eV and J_i decreased significantly to 0.05 A m^{-2} (figure 8(g)). Due to the low $\overline{V_s}$ and J_i, L_{sh} was much lower than in the case of the conducting electrode. For these parameters we found $L_{sh} = 4$ mm and $\tau_i/\tau_{RF} \approx 17$. The measured ion energy distribution agrees with the simulation results as can be observed in figure 8(g). The IEDF at the powered electrode as obtained by the simulations resulted in a single bimodal peak centered at $\overline{V_s}$ of 186 V and ΔE of 9 eV was found. The peak of the distribution corresponds to the ion energy of $e(\overline{V_p} - V_{DC})$ due to development of a negative V_{DC} on the electrode. As shown in figure 9(b), in this case no electric field reversal develops in front of the powered electrode as due to the lower plasma potential a fair amount of electrons can leave the bulk plasma to the grounded walls and diffusion is sufficient during the local sheath collapse at the powered electrode to ensure charge balance, in contrast to the previous case.

The simulations with varying area ratios A_g/A_p were also performed for the insulating electrode. The plasma properties remained unaltered with changing A_g/A_p. The results are presented in figure A2 of the appendix.

4.3. Hybrid electrodes

Whenever a part of the surface is conducting, DC current is allowed to flow through the plasma and the application of the notch filter has an effect on the discharge characteristics. Therefore, for all hybrid electrodes the plasma potential is significantly higher than that for the electrode with a completely insulating surface that leads to the development of a high negative self-bias voltage.

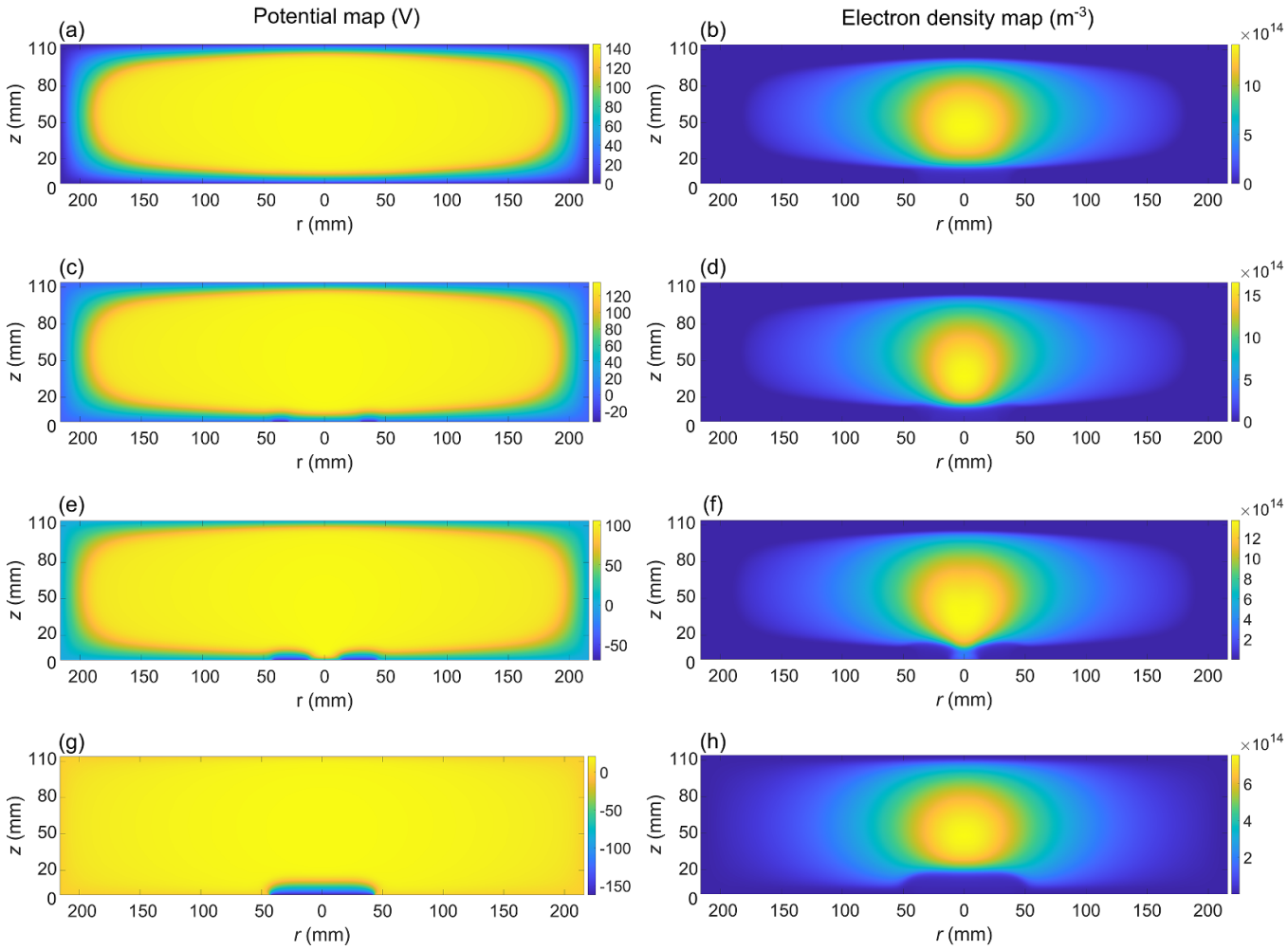

Figure 10. Time averaged electric potential and electron density distributions in the cross section of the discharge. Note that the simulation considers a cylindrically symmetric configuration. The powered electrode is at $z = 0$ mm with a radius $r = 42.5$ mm. All other surfaces are grounded. The results are shown for electrodes with different percentages of the conducting surface area: (a), (b) 100%, (c), (d) 50%, (e), (f) 10%, and (g), (h) 0%. The potential is given in units of volts and the density in units of m^{-3}.

As there is a net current through the electrode, $\overline{V_\mathrm{p}}$ can be described by equation (2). Due to the presence of V_DC at the electrode, L_sh at the wall and at the powered electrode are different. Moreover, the net capacitance at the powered electrode is a function of the radius of the electrode ($C_\mathrm{p} = C_\mathrm{p}(r)$), due to the presence of DC self-bias and DC grounding on different sections of the same electrode.

However, since the A_g is still much higher than A_p, the ratio of capacitances $C_\mathrm{g}/(C_\mathrm{p} + C_\mathrm{g})$ in equation (2) remains close to 1. As a result, the change in $\overline{V_\mathrm{p}}$ in equation (2) is mainly driven by the change in V_DC. Furthermore, since $C_\mathrm{g}/(C_\mathrm{p} + C_\mathrm{g})$ remains close to 1, the difference $\overline{V_\mathrm{p}} - V_\mathrm{DC}$ remains nearly a constant for same applied V_RF from equation (2).

For the electrode with 50% conducting surface a plasma potential of +143 V was obtained. This is lower when compared to that obtained with the electrode with fully conducting surface (+156 V), but still much higher compared to the case of the electrode with 0% conducting surface (for which $\overline{V_\mathrm{p}} = 18.5$ V). Further, the I_p drawn through the electrode (as measured by the current sensor) was 14 mA and the measured n_e and T_e were 1.55×10^{15} m^{-3} and 3.4 eV, respectively. The plasma characteristics are in good agreement with those obtained from the simulations as can be observed in figure 7. The simulation results also show the development of $V_\mathrm{DC} = -38$ V on the insulating portion of the electrode (figure 10(c)) in addition to a high n_e on the conducting portion (figure 10(d)).

The ion energy distribution, computed for the total (powered) electrode surface (i.e. not resolving the differences between the conducting and insulating portions of the surface) therefore display two bimodal energy peaks with ΔE of 10 eV (figure 8(d)), one centered around 172 eV, corresponding to an ion energy of $e(\overline{V_\mathrm{p}} - V_\mathrm{DC})$ and the other around 134 eV corresponding to an ion energy of $e\overline{V_\mathrm{p}}$. The amplitudes of these peaks (proportional to the ion current density) are nearly the same, corresponding to the equal conducting/insulating surface areas on the electrode. Furthermore, the IEDF computed for the total electrode was also decomposed to obtain independent IEDFs at the conducting and insulating surfaces. As can be inferred from figure 11, the IEDF for the hybrid electrode is

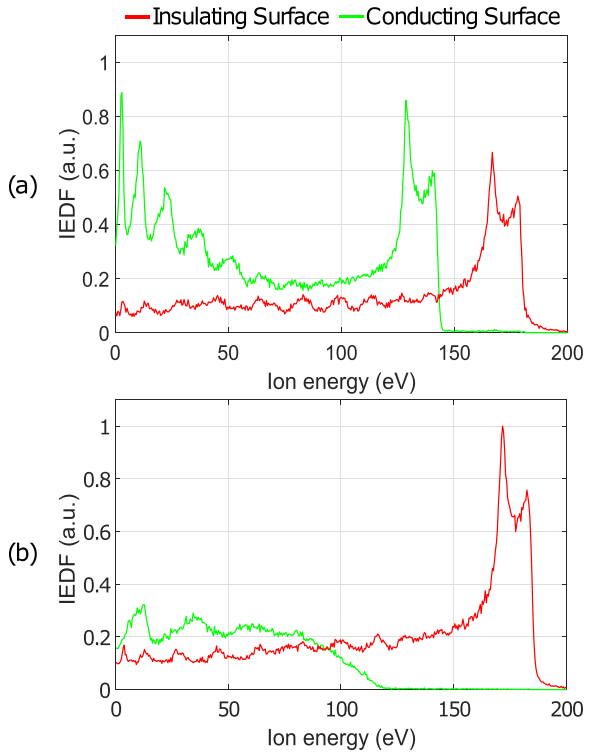

Figure 11. Decomposition of the (normalized) IEDF computed for the hybrid electrodes as observed in figures 8(d) and (f), to obtain the independent contributions at the insulating and conducting surface of the (a) 50% conducting and (b) 10% conducting electrode.

spatially dependent, since the lower energy bimodal peak (at 134 eV) was obtained almost entirely at the conducting surface of the electrode, while the higher energy peak (at 172 eV) was obtained at the insulating surface. The results obtained from the simulations are, to our knowledge, the first ever showing that different ion energy distributions can be obtained at a single electrode exhibiting different local material properties.

At the wall, the IEDF exhibits a single peak at 137.8 eV in good agreement with the corresponding simulation results (figure 8(c)). L_{sh} at the wall was found to be 13 mm due to the high $\overline{V_p}$ and τ_i/τ_{RF} was $\sim$20, similar to that in the case of the 100% conducting electrode.

With the electrode having 10% conducting surface area (figure 3(c)) $\overline{V_p}$, I_p and n_e decreased to +115 V, 11 mA and 1.2×10^{15} m^{-3}, respectively, while T_e remained at 3.2 eV. The decrease of $\overline{V_p}$ and n_e follows the trends obtained by the simulations (figure 7). With the decreasing proportion of the conducting area of the electrode we observed a further reduction of the plasma potential and a more negative DC self-bias at the insulating part of the electrode surface, amounting to −74.1 V (figure 10(e)).

The computed IEDF at the powered electrode displays one well defined bimodal peak with ΔE of 10 eV (figure 8(f)) centered around 176 eV corresponding to ion energy of $e(\overline{V_p} - V_{DC})$. This peak is obtained at the insulating surface of the electrode as observed in figure 11(b). The other peak that corresponded to ion energy of $e\overline{V_p}$ was not well defined. The disappearance of this peak can be explained on the basis of a statistical reduction in the ion current density at the conducting portion of the electrode which in this case is only 10% of the total surface. The behavior of IEDF at the electrode, as a result, is similar to the one observed for the electrode with insulating surface. This also implies, that the peak in the IEDF corresponding to $e\overline{V_p}$ gradually disappears as the percentage of the conducting surface of the electrode decreases.

At the grounded wall, the experimental IEDF has a single peak at 111 eV while J_i corresponding to the IEDF was 0.06 A m^{-2}. The IEDF peak obtained in the simulations was shifted to a lower energy of 101.5 eV, which is due to a 10 V lower $\overline{V_p}$ obtained in the simulations compared to the experiments (figure 8(e)). However, the behavior of the two curves is identical. Since $\overline{V_p}$ was still considerably high, L_{sh} at the wall was 12 mm which was a millimeter lower than the one calculated for the 100% and 50% conducting electrodes. τ_i/τ_{RF} at the wall was 21, which is also close to that for the electrodes with 100% and 50% conducting area.

From figure 7, it can be observed that the presence of conducting surface in any proportion on the powered electrode has a significant impact on the plasma properties, particularly V_p, T_e and L_{sh}, when compared to a purely insulating electrode, indicating that the flow of an electron current from plasma to the powered electrode dramatically influences the plasma properties. From figure 10, it can be observed that for both the hybrid electrodes, the potential varied over the electrode surface: the conducting part has a potential that corresponds to the excitation voltage, whereas the potential on the insulating part is defined by the balance between the charging of the electrons/positive ions. Although the discharge had a large radial extent, the volume with the highest electron density was confined to the inner part of the plasma, 'above' the electrode surface. Further, the simulation results indicate that the difference $\overline{V_p} - V_{DC}$ remains nearly the same for both hybrid electrodes (173.9 V for 50% and 179.1 V for 10%) and close to V_{RF} complementing equation (2).

In the case of electrodes with 100% conducting and 100% dielectric areas, global circuit models can be defined for the discharge, which can aid understanding of the voltage balance in these settings. In the case of hybrid electrodes, however, the definition of such a circuit model seems to be problematic as the system cannot be described by the parallel connection of the two circuits representing the conducting/insulating parts of the powered electrode. This is so because in the non-local regime of operation a significant and spatially distributed interplay between these two parts of the discharge is contemplated, and we do not expect that this can be represented by a small number of equivalent circuit elements.

5. Conclusion and outlook

The impact of DC grounding of the powered electrode with a quarter-wavelength notch filter on the plasma properties was investigated experimentally and numerically in a low pressure CCP source. Electrodes with different surface conducting properties (purely conducting, insulating and hybrid surfaces) were used in measurements of the electron density,

the plasma potential, the electron temperature (using a Langmuir probe) and the energy distribution of the positive ions reaching the grounded chamber wall (using an RFEA). In parallel, PIC/MCC simulations were performed for the different powered electrodes. The experimental results are in good agreement with the simulation outcomes for all the electrode configurations tested. Changing the conducting area of the powered electrode significantly influenced the properties of the plasma. The plasma potential increased to the order of the RF voltage amplitude in the case of the conducting electrode (147 V), while the electrode itself had a zero self-bias due to the DC grounding. In the case of the electrode covered with an insulating dielectric, there was no flow of DC current through the electrode and the effect of DC grounding was not observed. The plasma potential remained low and a high negative self-bias (-167 V as obtained from the simulations) developed on the surface. The properties of plasma were identical for the insulating electrode when driven with or without DC grounding with the notch filter.

Hybrid electrodes with 50% and 10% conducting surfaces led to combination of properties of both conducting and insulating electrodes. The conducting surface of the hybrid electrodes led to flow of a net DC current from the plasma to the electrode and a high resulting plasma potential, while the insulating surface led to the development of a negative self-bias on the part of the electrode that it covered. Changing the conducting area from 50% to 10% resulted in an increase of the negative self-bias voltage from -37.9 to -74.1 V while the plasma potential decreased from 143.1 to 115 V. The IEDFs for the electrode with 50% conducting area exhibited two well defined ion energy peaks corresponding to ion energies of $e(\overline{V_{\mathrm{p}}} - V_{\mathrm{DC}})$ at the insulating surface and $e\overline{V_{\mathrm{p}}}$ at the conducting surface of the electrode, respectively. For the electrode with 10% conducting area, most of the ions arrived at the electrode with the energy of $e(\overline{V_{\mathrm{p}}} - V_{\mathrm{DC}})$ leading to one well defined peak. The other peak, however, was not very well defined implying that the density of the peak corresponding to $e\overline{V_{\mathrm{p}}}$ decreases as the percentage of the conducting surface on the electrode is decreased. The IEDF at the electrode with 10% conducting area was also similar to that of the insulating electrode.

The results presented here are promising for the application of plasma cleaning with DC-grounded electrodes. With the conducting electrode, the plasma potential is high and uniform leading to an IEDF that peaks at a similar energy both at the wall and the electrode. This implies that, while the high ion energy would result in an effective sputtering of the electrode's surface (mirror), it would lead to an equivalent sputtering of the walls (considering the wall and electrode are made of the same material) leading to considerable re-deposition of the wall material on the electrode. This would significantly degrade the efficiency of net cleaning of the electrode's surface over time. Even if the wall and electrode's surface are made of different materials, a high plasma potential increases the likelihood for the ion energy to be higher than the sputtering threshold of the wall material. Consequently, the wall would be sputtered with a subsequent re-deposition on the powered electrode, hindering the mirror cleaning process. However, covering the conducting electrode with a thick dielectric results in a lowering of the plasma potential and a development of a negative self-bias on the mirror despite DC-grounding. As a result, the electrode's surface is sputtered with a significantly higher ion energy compared to that on the walls, ensuring a net cleaning of the electrode over time. The result is of significant importance for the metallic FMs in ITER diagnostics, where they are foreseen to undergo RF plasma cleaning while being DC-grounded with quarter-wavelength notch filter.

The results also show that the plasma properties obtained with an insulating electrode in presence of a notch filter are effectively similar to those obtained with a conducting electrode in a regular CCP (without DC grounding), with the major difference being that the charging occurs at the plasma surface interface in the former instead of the matching network or blocking capacitor. This points to implications when using RF plasmas (such as in semiconductor etching and PECVD) where addition of DC grounding can impact the plasma properties. Particularly, this calls for further exploration into the role of dielectric films in the plasma physics and the plasma surface interactions in CCPs, since the DC self-bias in such discharges is determined by both discharge asymmetry and the dielectric properties of the films. The DC grounded system, however, can pose complications when using multi-frequency waveforms, particularly when the DC grounding is achieved using a notch filter, since the length of the notch filter is determined by the RF frequency. We contemplate, however, that multi-frequency 'grounding networks' can as well be developed based on the same principles like multi-frequency matching networks [65].

The results with the DC-grounded hybrid electrodes show that the electrode is sputtered with two discrete ion energies $e\overline{V_{\mathrm{p}}}$ and $e(\overline{V_{\mathrm{p}}} - V_{\mathrm{DC}})$. This ion energy distribution has a spatial dependence, since the ion energy $e\overline{V_{\mathrm{p}}}$ is obtained primarily at the conducting portion of the electrode while the ion energy $e(\overline{V_{\mathrm{p}}} - V_{\mathrm{DC}})$ is obtained primarily at the dielectric region. This can be of interest for applications in the field of plasma-surface interactions that target selective sputtering of the electrode surface. Furthermore, the results indicate that the ratio of the dielectric to conducting surfaces on the powered electrode can highly impact the plasma properties. This property can find applications in the reactor designs of other CCPs with DC grounded electrodes, wherein the ratio of dielectric to conducting surfaces can be varied to tune the plasma parameters as well as the DC self-bias on the dielectric surface. This also calls for further research into how different dielectric materials can potentially influence the plasma properties, DC self-bias and eventually, the choice of the reactor design. The range of the ratio of conducting and dielectric surfaces on the electrode where the IEDF shifts from having two discrete ion energies ($e\overline{V_{\mathrm{p}}}$ and $e(\overline{V_{\mathrm{p}}} - V_{\mathrm{DC}})$) to a largely single ion energy is also a highly relevant topic for future study.

Moreover, our study deals with only asymmetric discharges, since $A_{\mathrm{g}}/A_{\mathrm{p}} \sim 80$. However, the results obtained also call for further studies into DC grounded discharges in more

symmetric systems ($A_g/A_p \sim 1$), with a particular emphasis on hybrid electrodes where the dielectric layer as well the sheath dynamics could have a prospective influence on the potential profile.

In the future, we will study the erosion of the electrode surfaces as a result of the dual ion energies on hybrid electrodes.

Acknowledgments

The authors would like to thank Michael Steinacher and the electronic workshop at University of Basel for their contribution toward building of the peak-to-peak voltage measurement device as well as for assisting in floating up the Langmuir probe to a DC potential used in the experiments. The authors would also like to thank the mechanical workshop at University of Basel for their contribution toward building of the components used in the experimental setup. This work has been carried out within the framework of the EUROfusion Consortium and has received funding from the Euratom research and training programme 2014–2018 and 2019–2020 under Grant Agreement No. 633053. The views and opinions expressed herein do not necessarily reflect those of the European Commission. The Swiss Federal Office of Energy, Swiss Nanoscience Institute, Swiss National Science Foundation and the Federal Office for Education and Science are acknowledged for their financial support. Zoltan Donko and Peter Hartmann acknowledge the financial support by the National Office for Research, Development and Innovation (NKFIH) of Hungary via Grant Nos. 134462 and 132158. Zoltan Juhasz would like to thank NVIDIA Corp. and their GPU Grant Program for the generous donation of a Titan Xp GPU card.

Appendix A.

This appendix presents some of the supplementary simulations results of the effects of a varying ratio of the areas of the grounded vs. the powered electrode.

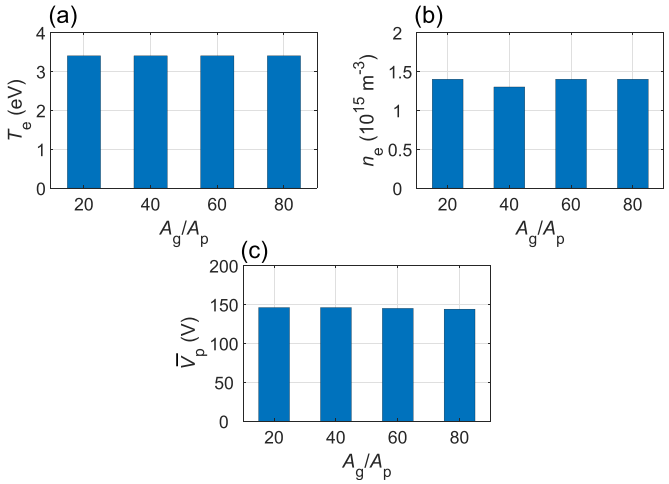

Figure A1. (a) Plasma potential $\overline{V_p}$, (b) electron density n_e and (c) electron temperature T_e with a conducting driven electrode as obtained by simulations for varying area ratio of the electrodes A_g/A_p. The area of the driven electrode A_p is kept constant, while the area of the grounded electrode A_g is varied to change the ratio A_g/A_p. The plasma parameters pertaining to the results are shown in table 3.

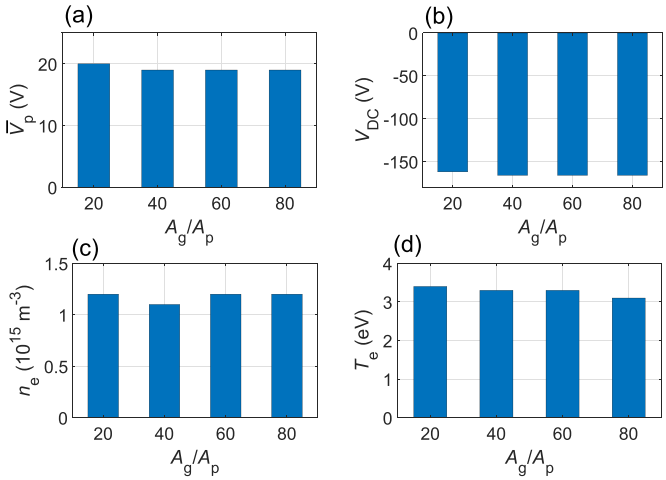

Figure A2. (a) Plasma potential $\overline{V_p}$, (b) self-bias V_{DC} on the electrode, (c) electron density n_e and (d) electron temperature T_e with an insulated electrode as obtained by simulations for varying area ratio of the electrodes A_g/A_p. The area of the driven electrode A_p is kept constant, while the area of the grounded electrode A_g is varied to change the ratio A_g/A_p. The Ar pressure used was 1.5 Pa.

ORCID iDs

Kunal Soni https://orcid.org/0000-0002-8786-7365
Lucas Moser https://orcid.org/0000-0003-1766-9942
Zoltán Donkó https://orcid.org/0000-0003-1369-6150
Peter Hartmann https://orcid.org/0000-0003-3572-1310
Ihor Korolov https://orcid.org/0000-0003-2384-1243
Rodrigo Antunes https://orcid.org/0000-0001-9993-7247
Zoltan Juhasz https://orcid.org/0000-0003-0677-8588
Roland Steiner https://orcid.org/0000-0002-4350-4132
Laurent Marot https://orcid.org/0000-0002-1529-9362
Ernst Meyer https://orcid.org/0000-0001-6385-3412

References

[1] Lieberman M A and Lichtenberg A J 2005 *Principles of Plasma Discharges and Materials Processing* (Hoboken, NJ: Wiley)
[2] Chabert P and Braithwaite N 2011 *Physics of Radio Frequency Plasmas* (Cambridge: Cambridge University Press)
[3] Makabe T and Lj Petrovic Z 2006 *Plasma Electronics: Applications in Microelectronic Device Fabrication* (London: Taylor and Francis)
[4] Schulze J and Mussenbrock T 2016 Electron heating in technological plasmas *Plasma Source Sci. Technol.* **25** 020401
[5] Wild C and Koidl P 1989 Structured ion energy distribution in radio frequency glow-discharge systems *Appl. Phys. Lett.* **54** 505–7
[6] Wild C and Koidl P 1991 Ion and electron dynamics in the sheath of radio-frequency glow discharges *J. Appl. Phys.* **69** 2909–22
[7] Donkó Z, Schulze J, Czarnetzki U, Derzsi A, Hartmann P, Korolov I and Schuengel E 2012 Fundamental investigations of capacitive radio frequency plasmas: simulations and experiments *Plasma Phys. Control. Fusion* **54** 124003
[8] Kitajima T, Takeo Y, Petrović Z L and Makabe T 2000 Functional separation of biasing and sustaining voltages in two-frequency capacitively coupled plasma *Appl. Phys. Lett.* **77** 849
[9] Boyle P C, Ellingboe A R and Turner M M 2004 Electrostatic modelling of dual frequency rf plasma discharges *Plasma Sources Sci. Technol.* **13** 493
[10] Czarnetzki U, Heil B G, Schulze J, Donkó Z, Mussenbrock T and Brinkmann R P 2009 The electrical asymmetry effect—a novel and simple method for separate control of ion energy and flux in capacitively coupled RF discharges *J. Phys.: Conf. Ser.* **162** 012010
[11] Lafleur T 2016 Tailored-waveform excitation of capacitively coupled plasmas and the electrical asymmetry effect *Plasma Sources Sci. Technol.* **25** 013001
[12] Diomede P *et al* 2014 Radio-frequency capacitively coupled plasmas in hydrogen excited by tailored voltage waveforms: comparison of simulations with experiments *Plasma Sources Sci. Technol.* **23** 065049
[13] Lafleur T *et al* 2013 Theory for the self-bias formation in capacitively coupled plasmas excited by arbitrary waveforms *Plasma Sources Sci. Technol.* **22** 065013
[14] Jiang W *et al* 2008 Heating mechanisms and particle flow balancing of capacitively coupled plasmas driven by combined dc/rf sources *Phys. Plasmas* **15** 033502
[15] Zhang Q-Z, Wang Y-N and Bogaerts A 2014 Heating mode transition in a hybrid direct current/dual-frequency capacitively coupled CF 4 discharge *J. Appl. Phys.* **115** 223302
[16] Cebulla R, Wendt R and Ellmer K 1998 Al-doped zinc oxide films deposited by simultaneous rf and dc excitation of a magnetron plasma: relationships between plasma parameters and structural and electrical film properties *J. Appl. Phys.* **83** 1087–95
[17] Li H *et al* 2003 Preparation and characterization of hydrogenated diamond-like carbon films in a dual DC-RF plasma system *J. Phys. D: Appl. Phys.* **36** 3183
[18] Faudot E *et al* 2019 Experimental measurements of the RF sheath thickness with a cylindrical Langmuir probe *Phys. Plasmas* **26** 083503
[19] Kim Y, Lee H and Chang H 2015 Micro-arc ignition on the oily surface of capacitively-coupled plasma *Curr. Appl. Phys.* **15** 313–8
[20] Dmitriev A M *et al* 2019 RF plasma cleaning of water-cooled mirror equipped with notch filter based on shorted $\lambda/4$ line *Fusion Eng. Des.* **146** 1390–3
[21] Lee J-R, Cho J-H and Yun S-W 2000 New compact bandpass filter using microstrip/spl lambda//4 resonators with open stub inverter *IEEE Microw. Guid. Wave Lett.* **10** 526–7
[22] Collins G A and Tendys J 1994 Measurements of potentials and sheath formation in plasma immersion ion implantation *J. Vac. Sci. Technol.* B **12** 875–9
[23] Köhler K *et al* 1985 Plasma potentials of 13.56-MHz rf argon glow discharges in a planar system *J. Appl. Phys.* **57** 59–66
[24] Köhler K, Horne D E and Coburn J W 1985 Frequency dependence of ion bombardment of grounded surfaces in rf argon glow discharges in a planar system *J. Appl. Phys.* **58** 3350–5
[25] Aanesland A *et al* 2005 Grounded radio-frequency electrodes in contact with high density plasmas *Phys. Plasmas* **12** 103505
[26] Aanesland A *et al* 2004 Helicon plasma with additional immersed antenna *J. Phys. D: Appl. Phys.* **37** 1334
[27] Yin Y *et al* 2004 Micro-arcing in radio frequency plasmas *J. Phys. D: Appl. Phys.* **37** 2871
[28] Yin Y *et al* 2005 Microarcing instability in RF PECVD plasma system *Surf. Coat. Technol.* **198** 379–83
[29] Yin Y, McKenzie D R and Bilek M M M 2006 Analytic analysis on asymmetrical micro arcing in high plasma potential RF plasma systems *Plasma Sources Sci. Technol.* **15** 99
[30] Sugai H, Nakamura K and Suzuki K 1994 Electrostatic coupling of antenna and the shielding effect in inductive RF plasmas *Japan. J. Appl. Phys.* **33** 2189
[31] Nakamura K, Kuwashita Y and Sugai H 1995 New inductive rf discharge using an internal metal antenna *Japan. J. Appl. Phys.* **34** L1686
[32] Litnovsky A *et al* 2019 Diagnostic mirrors for ITER: research in the frame of Int. Tokamak Physics Activity *Nucl. Fusion* **59** 066029
[33] Leipold F *et al* 2016 Cleaning of first mirrors in ITER by means of radio frequency discharges *Rev. Sci. Instrum.* **87** 11D439
[34] Soni K *et al* 2019 Plasma cleaning of steam ingressed ITER first mirrors *Nucl. Mater. Energy* **21** 100702
[35] Moser L *et al* 2015 Towards plasma cleaning of ITER first mirrors *Nucl. Fusion* **55** 063020
[36] Marot L *et al* 2013 Can aluminium or magnesium be a surrogate for beryllium: a critical investigation of their chemistry *Fusion Eng. Des.* **88** 1718–21
[37] Chen J L, Yan R and Xie H 2018 First mirror in-situ cleaning using radio frequency plasma on EAST for ITER edge Thomson scattering system *Proc. A3 Foresight Program Seminar on Critical Physics Issues Specific to Steady State*

Sustainment of High-Performance Plasmas (NIFS-PROC-109) (11–14 July, 2017, Sapporo, Japan) (Toki: National Institute for Fusion Science) pp 64–9
[38] Moser L 2017 Plasma cleaning of diagnostic first mirrors for the nuclear fusion machine ITER *PhD Thesis* University of Basel (https://edoc.unibas.ch/56229/1/Thesis_LucasMoser.pdf)
[39] de los Arcos T *et al* 2014 Description of HiPIMS plasma regimes in terms of composition, spoke formation and deposition rate *Plasma Sources Sci. Technol.* **23** 054008
[40] Chen F F 2003 Lecture notes on Langmuir probe diagnostics *IEEE-ICOPS Meeting (5 June 2003, Jeju, Korea)* (www.seas.ucla.edu/~ffchen/Publs/Chen210R.pdf)
[41] Španěl P 1995 An on-line Langmuir probe technique for the study of afterglow plasmas *Int. J. Mass Spectrom. Ion Process.* **149** 299–310
[42] Schulze J *et al* 2011 The electrical asymmetry effect in multi-frequency capacitively coupled radio frequency discharges *Plasma Sources Sci. Technol.* **20** 015017
[43] Gahan D *et al* 2012 Characterization of an asymmetric parallel plate radio-frequency discharge using a retarding field energy analyzer *Plasma Sources Sci. Technol.* **21** 015002
[44] Donko Z 2011 Particle simulation methods for studies of low-pressure plasma sources *Plasma Sources Sci. Technol.* **20** 024001
[45] Birdsall C K 1991 Particle-in-cell charged-particle simulations, plus Monte Carlo collisions with neutral atoms, PIC-MCC *IEEE Trans. Plasma Sci.* **19** 65–85
[46] Verboncoeur J P *et al* 1993 Simultaneous potential and circuit solution for 1D bounded plasma particle simulation codes *J. Comput. Phys.* **104** 321–8
[47] Vahedi V and Surendra M 1995 A Monte Carlo collision model for the particle-in-cell method: applications to argon and oxygen discharges *Comput. Phys. Commun.* **87** 179–98
[48] Tskhakaya D and Schneider R 2007 Optimization of PIC codes by improved memory management *J. Comput. Phys.* **225** 829–39
[49] Taccogna F *et al* 2007 Particle-in-cell simulation of stationary plasma thruster *Contrib. Plasma Phys.* **47** 635–56
[50] Tskhakaya D *et al* 2007 The particle-in-cell method *Contrib. Plasma Phys.* **47** 563–94
[51] Verboncoeur J P 2005 Particle simulation of plasmas: review and advances *Plasma Phys. Control. Fusion* **47** A231
[52] Yamabe C, Buckman S J and Phelps A V 1983 Measurement of free-free emission from low-energy-electron collisions with Ar *Phys. Rev.* A **27** 1345
[53] Phelps A V 1994 The application of scattering cross sections to ion flux models in discharge sheaths *J. Appl. Phys.* **76** 747–53
[54] Phelps A V 1991 Cross sections and swarm coefficients for nitrogen ions and neutrals in N2 and argon ions and neutrals in Ar for energies from 0.1 eV to 10 keV *J. Phys. Chem. Ref. Data* **20** 557–73
[55] Derzsi A *et al* 2015 Effects of fast atoms and energy-dependent secondary electron emission yields in PIC/MCC simulations of capacitively coupled plasmas *Plasma Sources Sci. Technol.* **24** 034002
[56] Evans D J 1984 Parallel SOR iterative methods *Parallel Comput.* **1** 3–18
[57] Klick M 1996 Nonlinearity of the radio-frequency sheath *J. Appl. Phys.* **79** 3445
[58] Schulze J, Kampschulte T, Luggenhölscher D and Czarnetzki U 2007 Diagnostics of the plasma series resonance effect in radio-frequency discharges *J. Phys.: Conf. Ser.* **86** 012010
[59] Sheridan T E 2000 How big is a small Langmuir probe? *Phys. Plasmas* **7** 3084–8
[60] Hershkowitz N, Cho M-H and Pruski J 1992 Mechanical variation of plasma potential, electron temperature and plasma density *Plasma Sources Sci. Technol.* **1** 87
[61] Hubble A A *et al* 2014 The electron spatial distribution and leak width in a magnetic cusp *Plasma Sources Sci. Technol.* **23** 022001
[62] Kawamura E *et al* 1999 Ion energy distributions in rf sheaths; review, analysis and simulation *Plasma Sources Sci. Technol.* **8** R45
[63] Child C D 1911 Discharge from hot CaO *Phys. Rev. (Ser. I)* **32** 492–511
[64] Langmuir I 1913 The effect of space charge and residual gases on thermionic currents in high vacuum *Phys. Rev.* **2** 450
[65] Schmidt F *et al* 2018 Multi frequency matching for voltage waveform tailoring *Plasma Sources Sci. Technol.* **27** 095012